A new parameterization scheme of the real part of the ambient urban aerosols refractive index

Gang Zhao[1], Tianyi Tan[2], Weilun Zhao[1], Song Guo[2], Ping Tian[3], Chunsheng Zhao[1*]

1 Department of Atmospheric and Oceanic Sciences, School of Physics, Peking University, Beijing, China

2 State Key Joint Laboratory of Environmental Simulation and Pollution Control, College of Environmental Sciences and Engineering, Peking University, Beijing 100871, China

3 Beijing Key Laboratory of Cloud, Precipitation and Atmospheric Water Resources, Beijing 100089, China

[*]**Correspondence to: Chunsheng Zhao (zcs@pku.edu.cn)**

Abstract

The refractive index of ambient aerosols, which directly determines the aerosol optical properties, is widely used in atmospheric models and remote sensing. Traditionally, the real part of the refractive index (RRI) is parameterized by the measurement of ambient aerosol main inorganic components. In this paper, the characteristics of the ambient aerosol RRI are studied based on the field measurement in the East China. The results show that the measured ambient aerosol RRI varies significantly between 1.36 and 1.56. The direct aerosol radiative forcing is estimated to vary by 40% when the RRI were varied between 1.36 and 1.56. We find that the ambient aerosol RRI is highly correlated with the aerosol effective density (ρ_{eff}) rather than the main chemical components. However, parameterization of the ambient aerosol RRI by ρ_{eff} are not available due to the lack of corresponding simultaneous field measurements. For the first time, the size-resolved ambient aerosol RRI and ρ_{eff} are measured

simultaneously by our designed measurement system. A new parameterization scheme of the ambient aerosols RRI using ρ_{eff} is proposed for the urban environments. The measured and parameterized RRI agree well with the correlation coefficient of 0.75 and slope of 0.99. Knowledge of the ambient aerosol RRI would improve our understanding of the ambient aerosol radiative effects.

1 Introduction

Atmospheric aerosols can significantly influence the regional air quality (An et al., 2019;Zhang et al., 2015). They change the climate system by scattering and absorbing the solar radiation (Seinfeld et al., 1998;Wang et al., 2013). However, estimation of the aerosol radiative effects remains large uncertainties due to the high temporal and spatial variations in aerosol microphysical properties (Levoni et al., 1997). The complex refractive index (RI), which directly determines the aerosol scattering and absorbing abilities (Bohren and Huffman, 2007), is one of the most important microphysical parameters of aerosol optics and radiation. RI is widely employed in atmospheric models and remote sensing (Zhao et al., 2017). When estimating the direct aerosol radiative forcing (DARF), many studies showed that great uncertainties may arise due to small uncertainties in the real part of the RI (RRI). It was found that a small perturbation in RRI (0.003) can lead to an uncertainty of 1% in DARF for non-absorbing particles (Zarzana et al., 2014). An increment of 12% in the DARF occurred when the RRI increased from 1.4 to 1.5 (Moise et al., 2015) over the wavelength range between 0.2 μm and 5 μm. Therefore, it is necessary to measure or parameterize the ambient aerosol RRI with high accuracy.

Traditionally, the RRI is derived from measurements of aerosol main inorganic chemical compositions (Han et al., 2009). For the ambient aerosol with multiple components, linear volume average of known aerosol chemical composition is widely used to estimate the aerosol effective RRI (Hand and Kreidenweis, 2002;Liu and Daum, 2008;Hänel, 1968;Wex et al., 2002) with :

$$RRI_{eff} = \sum_i (f_i \cdot RRI_i) \qquad (1)$$

Where f_i and RRI_i are the volume fraction and real part of refractive index of known composition *i*. However, the influences of organic component on the aerosol RRI were not considered when

estimating the RRI using the traditional method. The organic component contributes more than 20% of the total aerosol component in China (Hu et al., 2012;Liu et al., 2014). At the same time, RRI of the organic aerosol changes significantly between 1.36 and 1.66 (Moise et al., 2015). Ignoring the organic component may lead to significant biases when estimating the ambient aerosol RRI. The comparison between the estimated RRI using main aerosol composition and measured aerosol RRI using other method was not available due to the lack of measurement of ambient aerosol RRI.

Information of RRI may be helpful for the knowledge of ambient aerosol chemical information. Many studies find that ambient aerosols of different size have different properties such as shape (Peng et al., 2016), chemical composition (Hu et al., 2012) and density (Qiao et al., 2018). Up until now, there is limit information about the size-resolved RRI ($\widetilde{RRI}$, denoted in Table. S1) of ambient particles. Characteristics of the ambient aerosol $\widetilde{RRI}$ were not well studied yet.

The RRI of mono-component particle is defined as (Liu and Daum, 2008):

$$\frac{RRI^2-1}{RRI^2+2} = \frac{N_A \alpha}{3M} \rho_{eff} \qquad (2)$$

where N_A is the universal Avagadro's number, α is the mean molecular polarizability, M is the molecular weight of the material and ρ_{eff} is the mass effective density of the chemical component. The RRI should be highly related to ρ_{eff}. However, there was no study that investigated the relationship between the RRI and ρ_{eff} of ambient aerosol in China.

The ρ_{eff} of ambient aerosols is one of the crucial parameters in aerosol thermo-dynamical and optical models. It can be used to infer the ambient particle aging process (Peng et al., 2016). Based on equation 2, the aerosol ρ_{eff} is directly related to the aerosol RRI. Few studies measure the ambient aerosol RRI and ρ_{eff} simultaneously. So far, parameterizations of the RRI by ρ_{eff} using the simultaneous measurements are not available. Real-time measurements of the ρ_{eff} and aerosol RRI concurrently can help to better understand the relationship between the aerosol RRI and ρ_{eff}.

In this study, the aerosol $\widetilde{RRI}$ and size resolved ρ_{eff} ($\widetilde{\rho_{eff}}$) are measured simultaneously during a field measurement conducted in Taizhou in the East China. The ambient aerosol $\widetilde{RRI}$ is measured by our designed system, which combines a differential mobility analyzer (DMA) and a single particle soot photometer (SP2) (Zhao et al., 2019). The $\widetilde{\rho_{eff}}$ is measured by using a centrifugal particle mass analyzer (CMPA) and a scanning mobility particle sizer (SMPS). The characteristic of the $\widetilde{RRI}$ and

$\widetilde{\rho_{eff}}$ are analyzed in this study. It is the first time that the $\widetilde{RRI}$ and $\widetilde{\rho_{eff}}$ of the ambient aerosol are measured simultaneously. A parameterization scheme of the RRI by the ρ_{eff} using the simultaneous measurement is proposed. Based on the measured variability of the measured RRI, we estimated the corresponding variation of the aerosol direct aerosol radiative forcing, which to some extent give valuable knowledge for the influence of aerosol RRI variations on aerosol radiative effects.

The structure of this study is as follows: the descriptions of the instrument setup is given in section 2.1, 2.2 and 2.3. The methodology of evaluating the aerosol optical properties and radiative effects corresponding to the variations of the measured RRI are shown in section 2.4 and 2.5 respectively. Section 3.1 describes the characteristics of the measured $\widetilde{RRI}$ and $\widetilde{\rho_{eff}}$. Section 3.3 proposes the parameterization of the aerosol RRI. The corresponding variations in aerosol optical properties and radiative effects corresponding to the variations of the measured RRI are both discussed in section 3.4.

2 Data and Methods

2.1 Description of the measurement campaign

The measurement was conducted in a suburban site Taizhou (119°57'E, 32°35'N), as shown in fig. 1(a), which lies in the south end of the Jianghuai Plain in the central Eastern China. It is located on the north east of the megacity Nanjing with a distance of 118 km. Another megacity Shanghai is 200 km away from Taizhou in the southeastern direction. The industrial area between Nanjing and Shanghai has experienced severe pollutions in the past twenty years. The average Moderate Resolution Imaging Spectroradiometer (MODIS) aerosol optical depth data at 550nm over the year 2017, as shown in fig. 1(b), also reflects that the measurement site is more polluted than the surrounding areas.

During the field campaign, all of the instruments were placed in a container, in which the temperature was well controlled within 24±2 °C. The sample air was collected from a PM_{10} impactor (Mesa Labs, Model SSI2.5) mounted on the top of the container and then passed through a Nafion dryer tube to ensure that the relative humidity of the sample particles was controlled below 30%.

Along with the measurement of the $\widetilde{RRI}$ and $\widetilde{\rho_{eff}}$, the aerosol scattering coefficients (σ_{sca}) at three different wavelengths (450, 525 and 635 nm) were measured by an nephelometer (Aurora 3000, Ecotech, Australia) (Müller et al., 2011) at a resolution of 5 minutes. The scattering truncation and

non-Lambertian error was corrected using the same method as that of Ma et al. (2011). The aerosol water-soluble ions (NH_4^+, SO_4^{2-}, NO_3^-, Cl^-) of $PM_{2.5}$ were measured by an In situ Gas and Aerosol Compositions Monitor (TH-GAC3000, China). The mass concentration of elementary carbon and organic carbon (OC) of PM2.5 were measured using a thermal optical transmittance aerosol carbon analyzer (ECOC, Focused Photonics Inc.). The concentrations of Organic matters (OM) are achieved through multiplying OC concentration by 1.4 (Hu et al., 2012). The time resolution of the aerosol composition measurement was one hour.

Another field measurement were conducted in the campus of Peking University (PKU) (N39°59′, E116°18′), in North China Plain, where the aerosol effective density and real part of the refractive index are measured concurrently from 16th to 20st, December in 2018. More detail of this site can refer to (Zhao et al., 2018).

2.2 Measuring the $\widetilde{RRI}$

A coupling DMA-SP2 system was employed to measure the aerosol $\widetilde{RRI}$ from 24th, May to 18th, June in 2018. This system is introduced elsewhere by (Zhao et al., 2019) and a brief description is presented here. As schematically shown in fig. 2, the monodispersed aerosols selected by a DMA (Model 3081, TSI, USA) are drawn into a SP2 to measure the corresponding scattering properties. The SP2 is capable of distinguishing the pure scattering aerosols from the black carbon (BC) containing aerosols by measuring the incandescence signals at 1064 nm. For the pure scattering aerosol, the scattering strength (S) measured by SP2 is expressed as:

$$S = C \cdot I_0 \cdot (\sigma_{45^o} + \sigma_{135^o}) \qquad (3),$$

where C is a constant that is determined by the instrument response character; I_0 is the instrument's laser intensity; σ_{45^o} and σ_{135^o} is the scattering function of the sampled aerosol at 45° and 135°, respectively;. From Mie scattering theory, aerosol size and RRI directly determine the scattering function at a given direction. Inversely, the aerosol RRI can be retrieved when the aerosol size and scattering strength are determined. This system can measure the ambient aerosol $\widetilde{RRI}$ with uncertainty less than 0.02 (Zhao et al., 2019).

Before the measurement, this system is calibrated with ammonia sulfate (RRI=1.52). After calibration, ammonium chloride is used to validate the method of deriving the RRI at different aerosol

diameters. The RRI value of ammonium chloride is 1.642 (Lide, 2006) and the measured RRI of ammonium chloride is in the range between 1.624 and 1.656 in our study. Therefore, this measurement system can measure the ambient aerosol RRI with high accuracy.

2.3 Measuring the $\widetilde{\rho_{eff}}$

The $\widetilde{\rho_{eff}}$ is measured by a Centrifugal Particle Mass Analyzer (CPMA, version 1.53, Cambustion Ltd, UK) in tandem with a Scanning Mobility Particle Sizer (SMPS) system from 12th, June to 18th, June in 2018. The ρ_{eff} is defined as

$$\rho_{eff} = \frac{m_p}{\frac{\pi}{6} \times d_m^3} \qquad (4),$$

Where m_p is the particle mass and d_m is the aerosol mobility diameter selected by DMA.

The controlling of the CPMA-SMPS system is achieved by self-established Labview software. The CPMA is set to scan twelve different aerosol mass at 1.0, 1.4, 2.0, 2.9, 4.2, 5.9, 8.5, 12.1, 17.2, 24.6, 35.0 and 50.0 fg every five minutes respectively. The SMPS scan the aerosol diameters between 60nm and 500nm every 5 minute, which results in a period of one hour for measuring the effective density of different mass.

At the beginning of the field measurement, the CPMA-SMPS system is calibrated using the PSL particles with different mass. The corresponding measured effective densities of PSL particles are 1.04 and 1.07 g/cm^3, which agree well with the PSL material density of 1.05 g/cm^3.

Fig. 3 gave three examples of the aerosol PNSDs that passed the CPMA and were measured by the SMPS. The mass values of the aerosol that can pass through the CPMA were set to be 12, 1 and 1.4 fg respectively. From fig. 3, these aerosols that pass through the CPMA were mainly composed of three modes. For each mode, the aerosol number concentrations were fit by log-normal distribution function:

$$N(H) = \frac{N_0}{\sqrt{2\pi}\log(\sigma_g)} \cdot exp\left[-\frac{\log Dp - \log(Dp)}{2log^2(\sigma_g)}\right], \qquad (5)$$

where σ_g is the geometric standard deviation; Dp is the geometric mean diameter and N_0 is the number concentrations for a peak mode. The geometric mean diameter is further analyzed.

We would demonstrate the mode 1, 2 and 3 in fig. 3 correspond to those aerosols of absorbing aerosol, scattering aerosol, and scattering aerosol with double charges respectively.

Based on the principle of CPMA, when the CPMA is selecting the aerosols at mass m_0 of single charged aerosol particles. Theses multiple-charged (numbers of charges is *n*) aerosol particles with mass concentration of nm_0 can pass through the CPMA at the same time. We assumed that the geometric diameter of the single charge aerosol particles was D_0, and the effective density among different aerosol diameter didn't have significant variations. Thus, the geometric diameter of the multiple charged aerosol particles is $\sqrt[3]{n}$m.

As for the DMA, when a voltage (*V*) is applied to the DMA, only a narrow size range of aerosol particles, with the same electrical mobility (Z_p) can pass through the DMA (Knutson and Whitby, 1975). The Z_p is expressed as:

$$Z_P = \frac{Q_{sh}}{2\pi VL} ln(\frac{r_1}{r_2}) \quad (6)$$

where Q_{sh} is the sheath flow rate; *L* is the length of the DMA; r_1 is the outer radius of annular space and r_2 is the inner radius of the annular space. The aerosol $Z_{p,}$ which is highly related to the aerosols diameter (D_p) and the number of elementary charges on the particle (*n*), is defined as:

$$Z_p = \frac{neC(D_p)}{3\pi\mu D_p} \quad (7)$$

where *e* is the elementary charge; μ is the gas viscosity coefficient, $C(D_p)$ is the Cunningham slip correction that is defined by:

$$\mathrm{C} = 1 + \frac{2\tau}{D_p}(1.142 + 0.558e^{-\frac{0.999D_p}{2\tau}}) \quad (8)$$

where τ is the gas mean free path.

Therefore, the electrical diameter Zp(n) of the particles with n charges and diameters $\sqrt[3]{n}$m can be calculated based on equation 5. Thus, the corresponding diameter (Dn) measured by the DMA can be calculated with electrical diameter Zp(n) and single charged particle by using equation 5 again. The

178 relationship of the Dn and the aerosol diameter selected by the DMA can be determined by changing
179 the aerosol Dp and charge numbers. The results were shown in fig. 4.

180 The fit geometric diameters of mode 2 and mode 3 were also shown in fig. 4. From fig. 4, the
181 measured diameter relationships of the mode 2 and mode 3 agree well with the calculated one between
182 the single charged and double charged diameters. The little deviation might result from the
183 assumptions that the aerosol effective density doesn't change among different diameters. We
184 concluded that the mode 3 corresponds to the double-charged aerosols. Mode 3 is not used in our study.

185 Mode 1 and mode 2 corresponding to the effective densities around 1.0 g/cm^3 and 1.5 g/cm^3.
186 Previous studies have shown that the ambient BC aerosol was chain like in the morphology and had
187 smaller effective density values (Peng et al., 2016). At the same time, the fit aerosol number
188 concentrations of mode one is only between 1/5 to 1/3 of the mode two. Based on the size-selected
189 aerosol properties measured by the SP2, there were only mean 25% percent of the ambient aerosols
190 that contain BC. Therefore, the mode 1 and mode 2 corresponded to the BC-contained aerosols and
191 scattering aerosols respectively. There were some compacted BC-contained aerosols that may fit in
192 mode 2. We focus on the fit geometric mean diameter of mode 2, which corresponding to these
193 scattering aerosols that dominated this mode. Therefore, these compacted BC aerosols would not
194 influence our final conclusion.

195 The effective density used in our study correspond to the geometric diameters of mode 2. Thus,
196 both the measured aerosol ρ_{eff} and RRI correspond to these scattering aerosols

197 **2.4 Calculate aerosol optical properties using different RRI**

198 The aerosol optical properties are highly related to the RRI. From Mie scattering theory, the variation
199 in aerosol RRI may result in significant variations in the aerosol optical properties, such as aerosol
200 extinction coefficient (σ_{ext}), the $\sigma_{sca,}$ the single scattering albedo (SSA), and the asymmetry factor
201 (g) (Bohren and Huffman, 2007). The σ_{ext}, SSA and g are the most important three factors that
202 influence the aerosol radiative properties in radiative calculation (Kuang et al., 2015;Zhao et al., 2018).
203 In this study, the sensitivity studies of the aeorsol optical proprties to the aerosol RRI are carried
204 out by employing the Mie scattering theory. The input variables of Mie scattering model includes the

aerosol particle number size distriubiton (PNSD) and BC mixing state and aerosol complex refractive index. The Mie model can calculate the σ_{ext}, σ_{sca}, SSA and g. The mixing state of the ambient BC comes from the measurements of the DMA-SP2 system. All of the aerosols are divided into pure scattering aerosols and BC-containing aerosols. The BC-containing aerosols are assumed to be core-shell mixed. As for the RI of BC, 1.8+0.54i is used (Kuang et al., 2015). With this, the aerosol σ_{ext}, σ_{sca}, SSA and g at different RRI values can be calculated.

2.5 Estimating the aerosol DARF

In this study, the DARF under different aerosol RRI conditions is estimated by the Santa Barbara DISORT (discrete ordinates radiative transfer) Atmospheric Radiative Transfer (SBDART) model (Ricchiazzi et al., 1998). Under the cloud-free conditions, DARF at the TOA is calculated as the difference between radiative flux under aerosol-free conditions and aerosol present conditions (Kuang et al., 2016). The instant DARF value is calculated over the wavelength range between 0.25 μm and 4 μm.

Input data for the model are shown below. The vertical profiles of temperature, pressure and water vapor, which adopt the radiosonde observations at Taizhou site. The measured mean results corresponding the field measurement period are used. Vertical distributions of aerosol σ_{ext}, SSA and g with a resolution of 50 m, are resulted from the calculation using the Mie Model and parameterized aerosol vertical distributions. Methods for parameterization and calculation of the aerosol optical profiles can be found in Zhao et al. (2018). The surface albedo adopt the mean results of MODIS V005 Climate Modeling Grid (CMG) Albedo Product (MCD43C3) at the area of Taizhou from May, 2017 to April, 2018. The other default values are used in the simulation (Ricchiazzi et al., 1998).

3 Results and Discussions

3.1 The Measurements Results

The overview of the measurement is shown in fig. 5. During the measurement, the σ_{sca} is relatively low with a mean value of 167±74 Mm^{-1}. There were one major pollution episodes occurred based on the σ_{sca} time series as shown in fig. 5(a). This pollution happens on 13th, June and doesn't last long. The corresponding σ_{sca} reaches 540 Mm^{-1}. A moderate polluted condition between 14th, June and 15th, June is observed. The aerosol PNSD changes substantially with the pollution conditions as

shown in fig. 5(b). The geometric median aerosol diameter changes between 30 nm and 105 nm. The median diameter tends to be lower when the surrounding is cleaner. Despite the median diameter reaches 105 nm on 16th, June, the surrounding is relative clean due to the low aerosol number concentration. The $\widetilde{RRI}$ varies from 1.34 to 1.54 and the $\widetilde{\rho_{eff}}$ ranges between 1.21 to 1.80 g/cm^3 as shown in fig. 5 (c) and (d). From fig. 5, the measured RRI shows the same variation pattern with the $\rho_{eff.}$ Both the $\widetilde{RRI}$ and $\widetilde{\rho_{eff}}$ increase with the diameter, which may indicate that the aerosol chemical composition varies among different aerosol particle size.

As for the $\widetilde{RRI}$, the corresponding mean RRI values for aerosol diameter at 200 nm, 300 nm and 450 nm are 1.425±0.031, 1.435±0.041, 1.47±0.059. When comparing the probability distribution of the RRI for different diameter in fig. 6, the RRI is more dispersed when the particle size increases, implicating that the aerosol compositions become complicated when the aerosol get aged. Fig. 6 (a), (c) and (e) give diurnal variation of the $\widetilde{RRI}$ values at different particle sizes of 200 nm, 300 nm and 450 nm. The RRI shows diurnal cycles for different diameters. They reach the peak at about 15:00 in the afternoon and fall to the valley at around 9:00 in the morning.

The range of the measured RRI (1.34~1.56) is a little wider than the literature values. The past measurement of the ambient aerosol RRI values varies between 1.4 and 1.6 (Dubovik, 2002;Guyon et al., 2003;Zhang et al., 2016) over different measurement site. This is the first time that such high variations in ambient aerosol RRI were observed at one site.

The $\widetilde{\rho_{eff}}$ shows almost the same diurnal variations as the $\widetilde{RRI}$ as shown fig. S1. The diurnal variations of the $\widetilde{\rho_{eff}}$ is more dispersed because the time period of measuring the $\widetilde{\rho_{eff}}$ is shorter (7 days) comparing with the time of $\widetilde{RRI}$ (28 days). It is evident that the ρ_{eff} increased with particle size. The difference of ρ_{eff} among different particle size should be resulted from different contributions of chemical compositions, especially the OM. Based on the previous measurement of the size-resolved chemical compositions using a micro orifice uniform deposit impactors (MOUDI), the mass fraction of OM get decreased with the increment of aerosol diameter (Hu et al., 2012). At the same time, the effective density of OM is lower than the other main inorganic compositions.

3.2 Aerosol Chemical Composition versus the RRI

From equation (1) and (2), the aerosol RRI can be determined by aerosol chemical composition (Liu and Daum, 2008). Many studies calculate the RRI using the measurement results of the relative contributions of aerosol chemical composition (Yue et al., 1994;Hänel, 1968;Guyon et al., 2003;Stelson, 1990;Wex et al., 2002). However, there is no comparison between the RRI calculated from chemical composition and real-time measurement one until now. In this study, the relationship between the measured RRI and the mass fraction of each ion components is investigated.

As illustrated in fig. 7, The measured RRI have implicit relationship with the mass fraction of the σ_{sca} at 525 nm, OM, SO_4^{2-}, Cl^-, and NO_3^-. The mass ratio of NH_4^+ seems to be negatively correlated with the measured RRI. At the same time, the measured RRI values have no clear relationship with the absolute mass concentrations of the main aerosol chemical components, as shown in fig. S2.

The RRI is also calculated by applying the method proposed by Stelson (1990), in which the bulk chemical composition is used. The comparison between the calculated RRI and the measured RRI is shown in fig. 8. It can be noticed that the calculated RRI and the measured RRI doesn't agree well. There are several reasons that may cause the discrepancies. The first reason might be that the aerosol chemical information used in the method is the average mass of whole aerosol population. The aerosol chemical composition may vary significantly among different size. Secondly, the OM of the ambient aerosols is very complicated and the influence of the OM on the aerosol RRI has not been studied well. Therefore, more research is necessary when parameterizing the ambient aerosol RRI with the measured aerosol chemical composition.

We would demonstrate that the measured RRI at a given diameter of 300 nm is in consistent with that of the bulk aerosol optical properties derived RRI_{opt}. The aerosol-effective RRI of bulk aerosol was retrieved by applying the Mie scattering theory to the aerosol particle number size distribution (PNSD), aerosol bulk scattering coefficient and aerosol absorbing coefficient data (Cai et al., 2011). Fig. 9 shows the time series of measured RRI and retrived RRI_{opt}. Results in fig. 9 show that the measured RRI and retrieved RRI_{opt}shows good consistence with R^2= 0.58. Therefore, the measured size-resolved aerosol RRI can be used to represent the bulk aerosol optical properties. The measured RRI at 300 nm and calculated aerosol RRI using the bulk aerosol main chemical composition should

to some extent correlated with each other. However, as shown in fig. 8, the measured RRI at 300 nm and calculated RRI using the method of Stelson (1990) has R^2 of 0.07. Therefore, calculating the ambient aerosol RRI calculated using bulk aerosol main inorganic component may lead to great uncertainties.

3.3 Parameterizing the RRI using ρ_{eff}

As shown in fig. 5, there is good consistence between the variation of the measured $\widetilde{RRI}$ and $\widetilde{\rho_{eff}}$. When defining the specific refractive index Re with $Re = \frac{RRI^2-1}{RRI^2+2}$, we found that the Re is highly correlated with ρ_{eff} by a R^2 equaling 0.75 and slope 0.99 (fig. 10). The linear relationships between the Re and ρ_{eff} is:

$$\frac{RRI^2-1}{RRI^2+2} = 0.18\rho_{eff} \qquad (9).$$

The RRI can be calculated based on equation 6:

$$RRI = \sqrt{\frac{1+0.36\rho_{eff}}{1-0.18\rho_{eff}}} \qquad (10).$$

Based on equation 9 and fig. 10 the aerosol RRI can be parameterized by the ρ_{eff} with high accuracy and the uncertainties of the calculated RRI using equation 10 can be constrained within 0.025. The aerosol ρ_{eff} is easier to be measured, and equation 10 might be used as a good probe of parameterizing the RRI.

The RRI were also calculated using the parameterization scheme equation 9 with the field measurement data at PKU site. The slope and correlation coefficient at PKU site are 0.97 and 0.56 respectively. The calculated and measured RRI show good consistence. Therefore, this scheme is applicable for different seasons at both Center China and North China Plain. We also compared the measured RRI and calculated RRI using the measured ρ_{eff} that have been previously published (Hänel, 1968;Tang and Munkelwitz, 1994;Tang, 1996;Hand and Kreidenweis, 2002;Guyon et al., 2003). The measured and calculated RRI show good consistence with R^2 of 0.91 and slope of 1.0. Therefore, our parameterization scheme is universal and applicable for the urban aerosols.

This parameterization scheme is easy to use because the effective density is the only parameter used as input. We have demonstrated that the traditional method of calculating the RRI using aerosol main

chemical components can have significant bias because the effects of organic aerosol is not considered. The RRI can be easy to calculate based on our parameterization scheme, as the effective density of ambient aerosol is rather easier to measure.

In the previous, Liu and Daum (2008) summarized some of the measured RRI and the ρ_{eff}, and parameterized the RRI as

$$\frac{RRI^2-1}{RRI^2+2} = 0.23\rho^{0.39} \qquad (11).$$

The feasibility of this scheme is tested here and the results are shown in fig. 8. The measured and parameterized RRI using the method of Liu and Daum (2008) deviated from 1:1 line. The relationship of the effective density and RRI were mainly from 4000 pure materials and few ambient aerosol data. However, the ambient aerosol were far from pure materials. At the same time, most of the pure materials have negligible contribution to the total aerosol. Therefore, the parameterization scheme from Liu and Daum (2008) can't well describe the relationships of the effective density and RRI of ambient aerosol.

3.4 Influence of RRI Variation on Aerosol Optical Properties and Radiative Properties

The measured RRI varies between 1.34 and 1.56 during the field campaign. The corresponding aerosol optical properties are estimated. When estimating the aerosol optical properties with different aerosol RRI, the measured mean aerosol PNSD and mixing states are used. Fig. 11 gives the variation of the aerosol σ_{sca}, SSA and g. From fig. 11, the σ_{sca} varies from 162 Mm^{-1} to 308 Mm^{-1}. The SSA varies between 0.843 and 0.895, which matches the variations of the dry aerosol SSA for different aerosol size distributions in the North China Plain (NCP) (Tao et al., 2014). As for the aerosol g, it decreases from 0.667 to 0.602 with the increment of the aerosol RRI. The ambient g values in the NCP are found within 0.55 and 0.66 (Zhao et al., 2018). Thus, the variations of the RRI have significant influence on the g. The aerosol optical properties change significantly with the variation of the ambient aerosol RRI.

The instant DARF values under different RRI are also estimated and the results are illustrated in fig. 11(b). When the aerosol RRI increases from 1.4 to 1.5, the DARF varies from -6.17 to -8.35, corresponding to 15% variation in DARF. This values are in accordance with the work of Moise et al. (2015), who estimate that an increment of 12% in the DARF occurs when the RRI varies from 1.4 to

1.5. The DARF can change from -4.9 w/m^2 to -10.14 w/m^2 when the aerosol RRI increase from 1.34 to 1.56, which corresponding to 40% variation in DARF. Great uncertainties may arise when estimating the aerosol radiative forcing when using a constant RRI. The RRI should be different under different aerosol conditions. The real time measured RRI should be used rather than a constant RRI when estimating the ambient aerosol optical and radiative properties. However, the real-time measurement of ambient aerosol RRI is not available for most of the conditions. Therefore, parameterization of the ambient aerosol RRI is necessary.

4 Conclusions

The ambient aerosol RRI is a key parameter in determining the aerosol optical properties and knowledge of it can help constrain the uncertainties in aerosol radiative forcing. In this study, the ambient aerosol $\widetilde{RRI}$ were measured in East Chinafrom 24th, May to 18th, June in 2018. Results show that the ambient aerosol RRI varies over a wide range between 1.34 and 1.56. The RRI increases slowly with the increment of the aerosol diameter. The mean aerosol RRI values are 1.425±0.031, 1.435±0.041, 1.47±0.059 for aerosol diameter at 200 nm, 300 nm and 450 nm respectively. Probability distributions of the RRI show that the RRI is more dispersed with the increment of aerosol dimeter, which reflect the complexing aging processing of the ambient aerosol. The aerosol optical properties change significantly and the DARF is estimated to vary by 40% corresponding to the variation of the measured ambient aerosol RRI. The real-time measured RRI should be used rather than a constant RRI when estimating the ambient aerosol optical and radiative properties.

We find that the ambient aerosol RRI is highly correlated with the ρ_{eff} rather than the main chemical compositions of aerosols. There is discrepancy between the measured and parameterized RRI using the concurrently measured main chemical inorganic compositions of ambient aerosol. This might be resulted from two reasons. The first one is that the aerosol chemical information used for calculation is the total aerosol loading as the aerosol chemical compositions may change significantly among different size. Another one is that the influence of OM of ambient aerosols is not considered. The RRI of OM varies significantly for different compositions (Moise et al., 2015).

Despite that the RRI is correlated with the ρ_{eff}, parameterization scheme of the ambient aerosol RRI using ρ_{eff} is not available due to the lack of simultaneously measurement. For the first time, the $\widetilde{RRI}$ and $\widetilde{\rho_{eff}}$ were measured simultaneously using our designed system. A new parameterization scheme of the ambient aerosol RRI using the ρ_{eff} is proposed based on the field measurement results. The measured and parameterized RRI agree well with the correlation coefficient of 0.75 and slope of 0.99. This simple scheme is reliable and ready to be used in the calculation of aerosol optical and radiative properties. The corresponding measurement results can also be further used in climate model.

Competing interests. The authors declare that they have no conflict of interest.

Data availability. The data used in this study is available when requesting the authors.

Author contributions. GZ, CZ, WZ and SG designed and conducted the experiments; PT, TY and GZ discussed the results.

Acknowledgments. This work is supported by the National Natural Science Foundation of China (41590872) and National Key R&D Program of China (2016YFC020000:Task 5).

References

Aldhaif, A. M., Stahl, C., Braun, R. A., Moghaddam, M. A., Shingler, T., Crosbie, E., Sawamura, P., Dadashazar, H., Ziemba, L., Jimenez, J. L., Campuzano-Jost, P., and Sorooshian, A.: Characterization of the Real Part of Dry Aerosol Refractive Index Over North America From the Surface to 12 km, Journal of Geophysical Research: Atmospheres, 10.1029/2018jd028504, 2018.

An, Z., Huang, R.-J., Zhang, R., Tie, X., Li, G., Cao, J., Zhou, W., Shi, Z., Han, Y., Gu, Z., and Ji, Y.: Severe haze in northern China: A synergy of anthropogenic emissions and atmospheric processes, Proceedings of the National Academy of Sciences, 116, 8657-8666, 10.1073/pnas.1900125116, 2019.

Bohren, C. F., and Huffman, D. R.: Absorption and Scattering by a Sphere, in: Absorption and Scattering of Light by Small Particles, Wiley-VCH Verlag GmbH, 82-129, 2007.

Cai, Y., Montague, D. C., and Deshler, T.: Comparison of measured and calculated scattering from surface aerosols with an average, a size-dependent, and a time-dependent refractive index, Journal of Geophysical Research, 116, 10.1029/2010jd014607, 2011.

Dubovik, O.: Variability of absorption and optical properties of key aerosol types observed in worldwide locations, J.atmos.sci, 59, 590-608, 2002.

Guyon, P., Boucher, O., Graham, B., Beck, J., Mayol-Bracero, O. L., Roberts, G. C., Maenhaut, W., Artaxo, P., and Andreae, M. O.: Refractive index of aerosol particles over the Amazon tropical forest during LBA-EUSTACH 1999, Journal of Aerosol Science, 34, 883-907, 10.1016/s0021-8502(03)00052-1, 2003.

Han, Y., Lü, D., Rao, R., and Wang, Y.: Determination of the complex refractive indices of aerosol from aerodynamic particle size spectrometer and integrating nephelometer measurements, Applied Optics, 48, 4108-4117, 10.1364/AO.48.004108, 2009.

Hand, J. L., and Kreidenweis, S. M.: A New Method for Retrieving Particle Refractive Index and Effective Density from Aerosol Size Distribution Data, Aerosol Sci. Technol., 36, 1012-1026, 10.1080/02786820290092276, 2002.

Hänel, G.: REAL PART OF MEAN COMPLEX REFRACTIVE INDEX AND MEAN DENSITY OF SAMPLES OF ATMOSPHERIC AEROSOL PARTICLES, Tellus, 20, 371-&, 10.3402/tellusa.v20i3.10016, 1968.

Hu, M., Peng, J., Sun, K., Yue, D., Guo, S., Wiedensohler, A., and Wu, Z.: Estimation of size-resolved ambient particle density based on the measurement of aerosol number, mass, and chemical size distributions in the winter in Beijing, Environ Sci Technol, 46, 9941-9947, 10.1021/es204073t, 2012.

Knutson, E. O., and Whitby, K. T.: Aerosol classification by electric mobility: apparatus, theory, and applications, Journal of Aerosol Science, 6, 443-451, https://doi.org/10.1016/0021-8502(75)90060-9, 1975.

Kuang, Y., Zhao, C. S., Tao, J. C., and Ma, N.: Diurnal variations of aerosol optical properties in the North China Plain and their influences on the estimates of direct aerosol radiative effect, Atmos. Chem. Phys., 15, 5761-5772, 10.5194/acp-15-5761-2015, 2015.

Kuang, Y., Zhao, C. S., Tao, J. C., Bian, Y. X., and Ma, N.: Impact of aerosol hygroscopic growth on the direct aerosol radiative effect in summer on North China Plain, Atmospheric Environment, 147, 224-233, 2016.

Levoni, C., Cervino, M., Guzzi, R., and Torricella, F.: Atmospheric aerosol optical properties: a database of radiative characteristics for different components and classes, Appl Opt, 36, 8031-8041, 1997.

Lide, D. R.: Handbook of Chemistry and Physics, 86th Edition Edited(National Institute of Standards and Technology), Journal of the American Chemical Society, 128, 5585-5585, 10.1021/ja059868l, 2006.

Liu, H. J., Zhao, C. S., Nekat, B., Ma, N., Wiedensohler, A., van Pinxteren, D., Spindler, G., Müller, K., and Herrmann, H.: Aerosol hygroscopicity derived from size-segregated chemical composition and its parameterization in the North China Plain, Atmospheric Chemistry and Physics, 14, 2525-2539, 10.5194/acp-14-2525-2014, 2014.

Liu, Y., and Daum, P. H.: Relationship of refractive index to mass density and self-consistency of mixing rules for multicomponent mixtures like ambient aerosols, Journal of Aerosol Science, 39, 974-986, 10.1016/j.jaerosci.2008.06.006, 2008.

Ma, N., Zhao, C. S., Nowak, A., Müller, T., Pfeifer, S., Cheng, Y. F., Deng, Z. Z., Liu, P. F., Xu, W. Y., Ran, L., Yan, P., Göbel, T., Hallbauer, E., Mildenberger, K., Henning, S., Yu, J., Chen, L. L., Zhou, X. J., Stratmann, F., and Wiedensohler, A.: Aerosol optical properties in the North China Plain during HaChi campaign: an in-situ optical closure study, Atmos. Chem. Phys., 11, 5959-5973, 10.5194/acp-11-5959-2011, 2011.

Moise, T., Flores, J. M., and Rudich, Y.: Optical properties of secondary organic aerosols and their changes by chemical processes, Chemical Reviews, 115, 4400-4439, 2015.

Müller, T., Laborde, M., Kassell, G., and Wiedensohler, A.: Design and performance of a three-wavelength LED-based total scatter and backscatter integrating nephelometer, Atmos. Meas. Tech., 4, 1291-1303, 10.5194/amt-4-1291-2011, 2011.

Peng, J., Hu, M., Guo, S., Du, Z., Zheng, J., Shang, D., Levy Zamora, M., Zeng, L., Shao, M., Wu, Y.-S., Zheng, J., Wang, Y., Glen, C. R., Collins, D. R., Molina, M. J., and Zhang, R.: Markedly enhanced

absorption and direct radiative forcing of black carbon under polluted urban environments, Proceedings of the National Academy of Sciences, 113, 4266-4271, 10.1073/pnas.1602310113, 2016.
Qiao, K., Wu, Z., Pei, X., Liu, Q., Shang, D., Zheng, J., Du, Z., Zhu, W., Wu, Y., Lou, S., Guo, S., Chan, C. K., Pathak, R. K., Hallquist, M., and Hu, M.: Size-resolved effective density of submicron particles during summertime in the rural atmosphere of Beijing, China, Journal of Environmental Sciences, 10.1016/j.jes.2018.01.012, 2018.
Ricchiazzi, P., Yang, S., Gautier, C., and Sowle, D.: SBDART: A Research and Teaching Software Tool for Plane-Parallel Radiative Transfer in the Earth's Atmosphere, Bulletin of the American Meteorological Society, 79, 2101-2114, 10.1175/1520-0477(1998)079<2101:sarats>2.0.co;2, 1998.
Seinfeld, J. H., Pandis, S. N., and Noone, K.: Atmospheric Chemistry and Physics: From Air Pollution to Climate Change, Environment Science & Policy for Sustainable Development, 40, 26-26, 1998.
Stelson, A. W.: Urban aerosol refractive index prediction by partial molar refraction approach, Environ.sci.technol, 24:11, 1676-1679, 1990.
Tang, I. N., and Munkelwitz, H. R.: WATER ACTIVITIES, DENSITIES, AND REFRACTIVE-INDEXES OF AQUEOUS SULFATES AND SODIUM-NITRATE DROPLETS OF ATMOSPHERIC IMPORTANCE, J Geophys Res-Atmos, 99, 18801-18808, 10.1029/94jd01345, 1994.
Tang, I. N.: Chemical and size effects of hygroscopic aerosols on light scattering coefficients, Journal of Geophysical Research: Atmospheres, 101, 19245-19250, 10.1029/96jd03003, 1996.
Tao, J. C., Zhao, C. S., Ma, N., and Liu, P. F.: The impact of aerosol hygroscopic growth on the single-scattering albedo and its application on the NO2 photolysis rate coefficient, Atmos. Chem. Phys., 14, 12055-12067, 10.5194/acp-14-12055-2014, 2014.
Wang, Y., Khalizov, A., Levy, M., and Zhang, R.: New Directions: Light absorbing aerosols and their atmospheric impacts, Atmospheric Environment, 81, 713-715, 10.1016/j.atmosenv.2013.09.034, 2013.
Wex, H., Neusüß, C., Wendisch, M., Stratmann, F., Koziar, C., Keil, A., Wiedensohler, A., and Ebert, M.: Particle scattering, backscattering, and absorption coefficients: An in situ closure and sensitivity

study, Journal of Geophysical Research: Atmospheres, 107, LAC 4-1-LAC 4-18, 10.1029/2000jd000234, 2002.

Yue, G. K., Poole, L. R., Wang, P. H., and Chiou, E. W.: STRATOSPHERIC AEROSOL ACIDITY, DENSITY, AND REFRACTIVE-INDEX DEDUCED FROM SAGE-II AND NMC TEMPERATURE DATA, J Geophys Res-Atmos, 99, 3727-3738, 10.1029/93jd02989, 1994.

Zarzana, K. J., Cappa, C. D., and Tolbert, M. A.: Sensitivity of Aerosol Refractive Index Retrievals Using Optical Spectroscopy, Aerosol Sci. Technol., 48, 1133-1144, 10.1080/02786826.2014.963498, 2014.

Zhang, G., Bi, X., Qiu, N., Han, B., Lin, Q., Peng, L., Chen, D., Wang, X., Peng, P., apos, an, Sheng, G., and Zhou, Z.: The real part of the refractive indices and effective densities for chemically segregated ambient aerosols in Guangzhou measured by a single-particle aerosol mass spectrometer, Atmospheric Chemistry and Physics, 16, 2631-2640, 10.5194/acp-16-2631-2016, 2016.

Zhang, R., Wang, G., Guo, S., Zamora, M. L., Ying, Q., Lin, Y., Wang, W., Hu, M., and Wang, Y.: Formation of urban fine particulate matter, Chemical Reviews, 115, 3803-3855, 2015.

Zhao, G., Zhao, C., Kuang, Y., Tao, J., Tan, W., Bian, Y., Li, J., and Li, C.: Impact of aerosol hygroscopic growth on retrieving aerosol extinction coefficient profiles from elastic-backscatter lidar signals, Atmospheric Chemistry and Physics, 17, 12133-12143, 10.5194/acp-17-12133-2017, 2017.

Zhao, G., Zhao, C., Kuang, Y., Bian, Y., Tao, J., Shen, C., and Yu, Y.: Calculating the aerosol asymmetry factor based on measurements from the humidified nephelometer system, Atmospheric Chemistry and Physics, 18, 9049-9060, 10.5194/acp-18-9049-2018, 2018.

Zhao, G., Zhao, W., and Zhao, C.: Method to measure the size-resolved real part of aerosol refractive index using differential mobility analyzer in tandem with single-particle soot photometer, Atmospheric Measurement Techniques, 12, 3541-3550, 10.5194/amt-12-3541-2019, 2019.

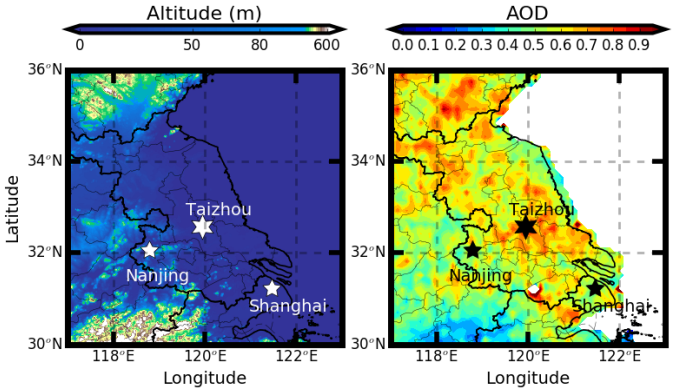

499

500 **Figure 1:** Measurement site of Taizhou (marked with stars). Filled colors represent (a) the

501 topography of the Jianghuai Plain. (b) the average aerosol optical depth at 550nm during the year of

502 2017 from Moderate Resolution Imaging Spectroradiometer onboard satellite Aqua.

503

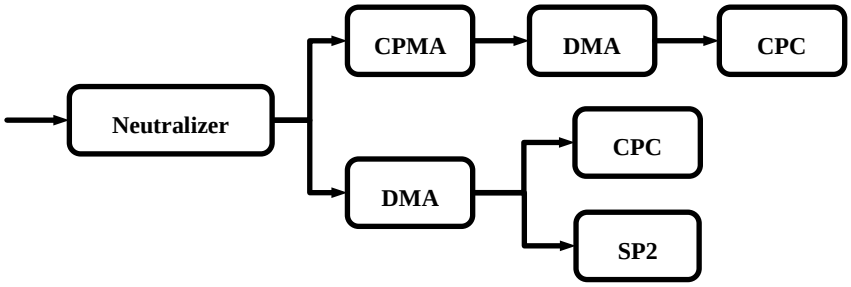

Figure 2. Schematic of the instrument setup.

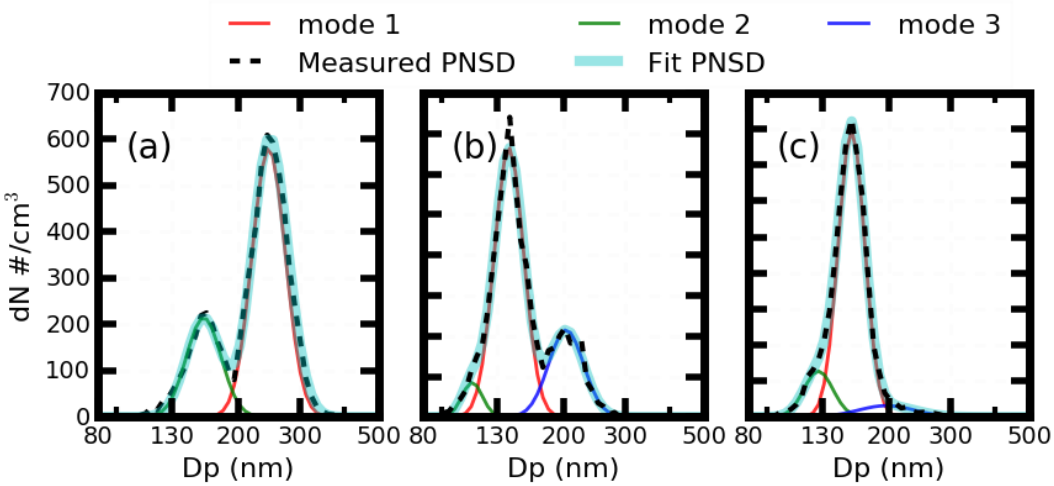

Figure 3. The measured aerosol PNSD (black dotted line), fit aerosol number PNSD (blue solid line), and fit aerosol PNSD at three different mode in different colors that passed through the CPMA. Panel (a) (b) (c) corresponding to the aerosol mass concentrations of 12, 1 and 1.45 fg respectively.

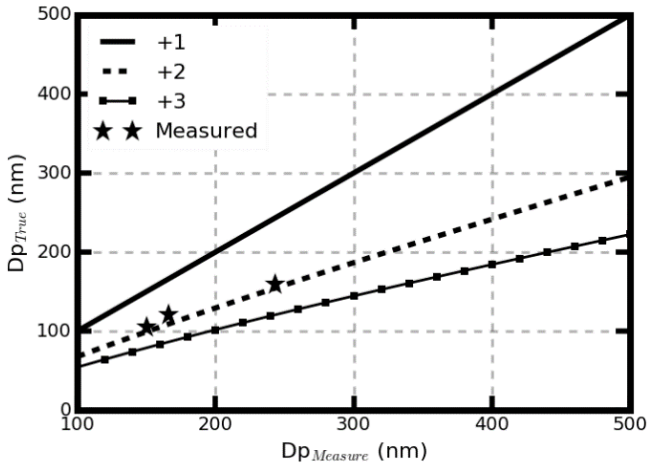

Figure 4. The relationship between the measured diameter by the DMA and the calculated aerosol diameter of different charges in the CPMA-SMPS system.

519

520

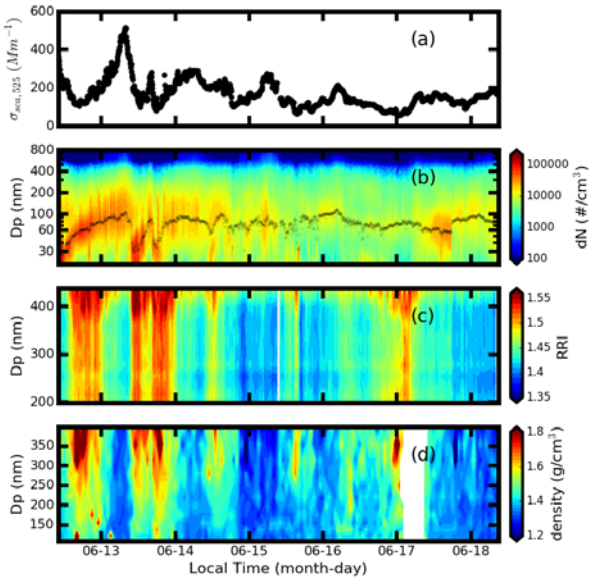

521

522 **Figure 5.** Time series of the measured (a) size-resolved RRI in filled color, σ_{sca} at 525nm in

523 black dotted line and (b) the size-resolved ρ_{eff}.

524

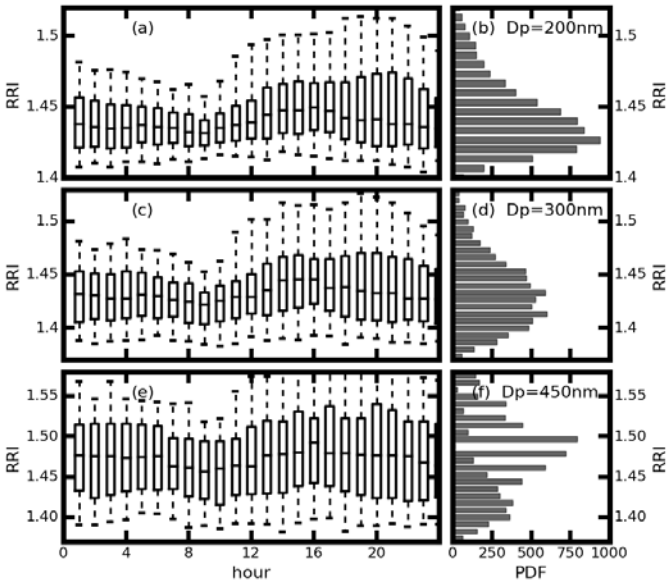

Figure 6. Daily variations of the RRI (a), (c) (e), and the probability distribution of the measured RRI (b), (d) (f) for the (a), (b) 200 nm, (c), (d) 300 nm, and (e), (f) 450nm aerosol respectively. The box and whisker plots represent the 5^{th}, 25^{th}, 75^{th} and 95^{th} percentiles.

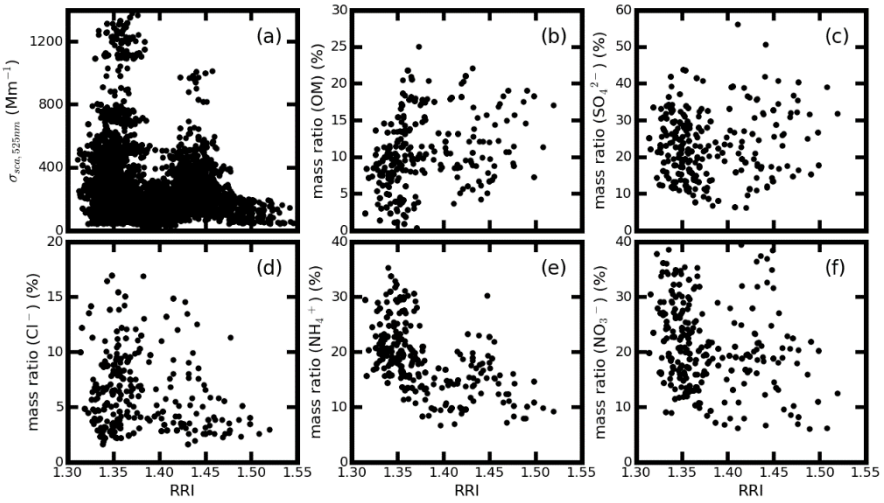

530

531 **Figure 7.** Comparison the measured RRI at 300nm with the measured (a) σ_{sca} at 525nm, mass

532 fraction of (b) OM, (c) SO_4^{2-}, (d) Cl^-, (e) NH_4^+ and (f) NO_3^-.

533

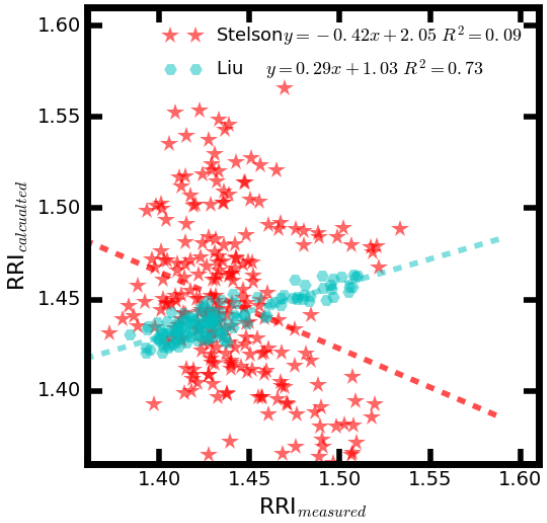

534

535 **Figure 8.** Comparison between the measured RRI and calculated RRI using the main aerosol
536 chemical component by applying the method of Stelson (1990) (in red star) and parameterization
537 scheme proposed by Liu and Daum (2008) (in cyan hexagon).

538

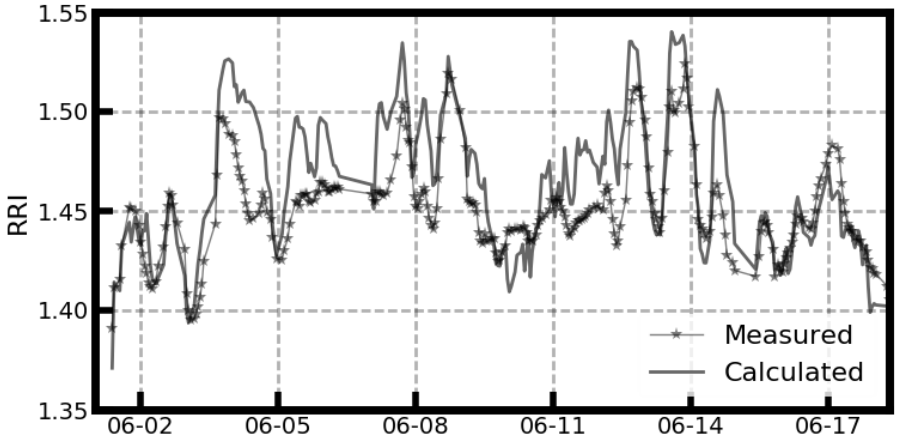

Figure. 9. Time series of the measured RRI at 300 nm and the calculated RRI using the aerosol bulk aerosol optical properties.

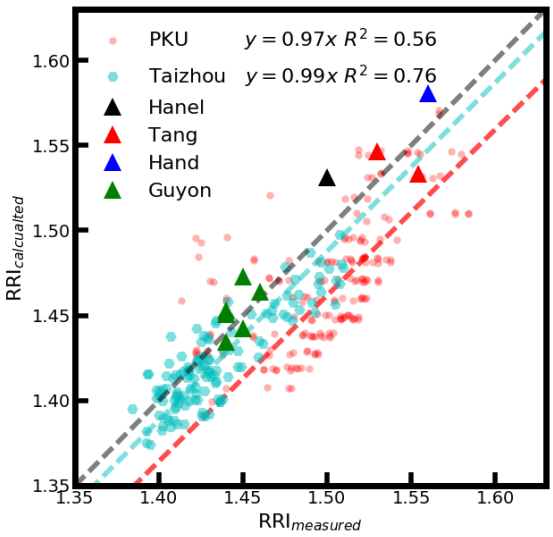

Figure 10. Comparison between the measured and calculated RRI for different at PKU (in red circle) and Taizhou (in cyan hexagon) station. The triangle in black , red, blue and green corresponding the data from Hänel (1968), Tang (1996), Hand and Kreidenweis (2002), and Guyon et al. (2003) respectively. The black dashed line is the 1:1 line.

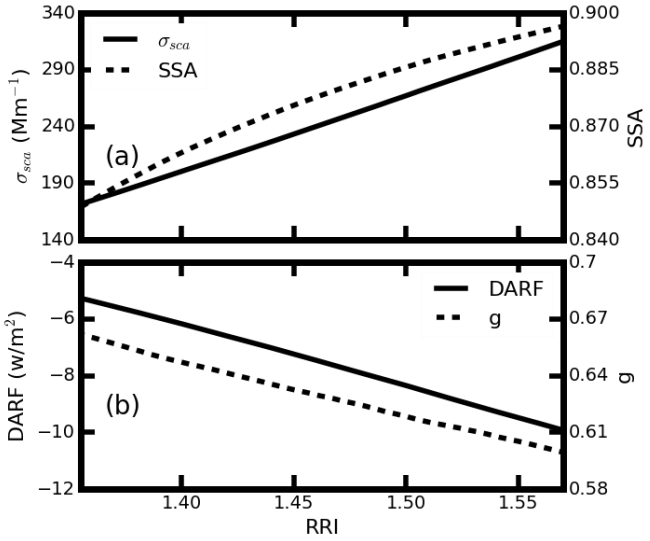

Figure 11. Variations of the estimated (a) σ_{sca} in solid line, SSA in dotted line, (b) g in dotted line, and DARF in solid line for different aerosol RRI.